Front. Struct. Civ. Eng. 2020, 14(4): 998–1011
https://doi.org/10.1007/s11709-020-0621-8

RESEARCH ARTICLE

Three-dimensional finite difference analysis of shallow sprayed concrete tunnels crossing a reverse fault or a normal fault: A parametric study

Masoud RANJBARNIA[a*], Milad ZAHERI[a], Daniel DIAS[b,c]

[a] *Department of Geotechnical Engineering, Faculty of Civil Engineering, University of Tabriz, Tabriz, Iran*

[b] *School of Automotive and Transportation Engineering, Hefei University of Technology, Hefei 230009, China*

[c] *Université Grenoble Alpes, Grenoble F-38000, France*

[*] *Corresponding author. E-mail: M.ranjbarnia@tabrizu.ac.ir*

ABSTRACT Urban tunnels crossing faults are always at the risk of severe damages. In this paper, the effects of a reverse and a normal fault movement on a transversely crossing shallow shotcreted tunnel are investigated by 3D finite difference analysis. After verifying the accuracy of the numerical simulation predictions with the centrifuge physical model results, a parametric study is then conducted. That is, the effects of various parameters such as the sprayed concrete thickness, the geo-mechanical properties of soil, the tunnel depth, and the fault plane dip angle are studied on the displacements of the ground surface and the tunnel structure, and on the plastic strains of the soil mass around tunnel. The results of each case of reverse and normal faulting are independently discussed and then compared with each other. It is obtained that deeper tunnels show greater displacements for both types of faulting.

KEYWORDS urban tunnel, sprayed concrete, reverse fault, normal fault, finite difference analysis

1 Introduction

The safe construction of urban tunnels against earthquake vibrations is an important issue. The problem is more highlighted when these tunnels are constructed in seismic areas. It is better to avoid constructing tunnels near active faults, but sometimes passing through a fault is even inevitable. In such cases, the moving of faults and subsequently deformation of tunnels are great concerns and can have remarkable effects on the stability of tunnels. In the Kobe earthquake in 1995 and the Chi-Chi earthquake in 1999, some tunnels experienced significant damages due to fault movements.

Most of studies in the earthquake engineering focused on the dynamic reaction of the soils and of the structures, and few studies are devoted to evaluate the effects of a moving fault on tunnels [1–5]. In some cases, the effects of faulting on the free field have been investigated [6–9]. In other attempts, the interaction between the faults and shallow or deep foundations has been studied by numerical methods as well as by centrifuge physical tests [10–15]. However, the problem of a fault rupture in constructed tunnels have been rarely studied.

Wang et al. [5] numerically investigated the effects of various faults movements on the flexible lining of tunnels. It was found the tunnel lining is seriously damaged for the case of strike-slip faulting. The aim of their study was the recognition of the potential risk of different faults, and the effects of different factors such as the rock mass parameters on the tunnel response were not evaluated. Baziar et al. [1] modeled the effects of the reverse fault movement on a tunnel by the finite element software ABAQUS and by the centrifuge tests. In their research, the fault plane was parallel to the tunnel longitudinal axis, and therefore; adoption of a 2D model was possible. It was assumed that the fault dip angle was 60° while the shotcrete was the support system. In the numerical simulation, the effects of different factors such as the friction angle and elastic modulus of soil, the shotcrete thickness and its elastic modulus, and the tunnel position

Article history: Received Apr 27, 2019; Accepted Jun 17, 2019

with respect to the fault were evaluated. The results show that the soil elastic modulus is the most critical parameter. However, the adopted numerical modeling was 2D and only one type of soil and one value for fault angle were considered in the tests. Kiani [16] studied the effects of a normal faulting on a segmental tunnel by centrifuge test where the fault dip angle was selected as 60° and 75°. The effects of the tunnel depth and the fault angle on the sinkhole dimensions as well as on the tunnel deformations were assessed. It was found that increasing the overburden of the tunnel and decreasing the angle of the fault lead the affected length of tunnel to be smaller. Due to some limitations associated to the centrifuge physical test, the effects of soil parameters and tunnel structure were not studied.

The literature review permits to show that the problem of tunnels crossing various faults in different conditions has not been sufficiently studied, and a need arises to comprehensively focus on this problem.

Studying the case of a tunnel transversely (perpendicularly) crosses a fault plane is of the great interest in urban areas. This problem has not been addressed. That is, the influence of spatial location of the fault plane with respect to the tunnel axis is investigated on tunnel response by three dimensional numerical simulations. The effects of ground geomechanical properties (dry sand with different densities), tunnel depth, lining thickness, and fault plane dip angle with respect to tunnel axis are evaluated on tunnel and on surface structures responses. The results of each case of reverse and normal faulting are first independently discussed and then compared with each other.

2 Finite difference modeling

2.1 General assumptions

To start the numerical study of the interaction between tunnel and active fault, several numerical approaches such as the finite difference method (e.g., the studies in Refs. [17–27]), the finite element method (e.g., the studies in Refs. [2,4]), and the mesh-less/mesh-free method which does not require a discretization like FDM and FEM methods (like studies in Refs. [28–30]) can be adopted. In this paper, the finite difference method by FLAC3D is used where the model consists of two parts, the foot wall and the hanging wall. These two parts are shown in Fig. 1.

To model the shearing mechanism between the two fault sides, an interface was introduced between the foot wall and the hanging wall. The shearing behavior of the interface is governed by a linear elastic perfectly plastic constitutive model (the Mohr-Coulomb criterion) where its strength properties, i.e., the friction angle, the dilation angle, and the cohesion are considered the same as the soil. The normal stiffness and the shear stiffness of the interface

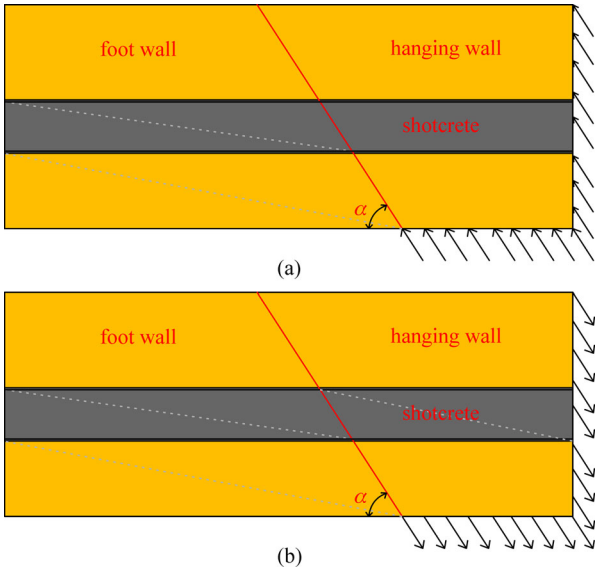

Fig. 1 Hanging wall and foot wall: (a) in the reverse fault; (b) in the normal fault.

were chosen ten times of the equivalent stiffness of Eq. (1) [31].

$$\max\left[\frac{K+\frac{4}{3}G}{\Delta z_{\min}}\right], \tag{1}$$

where K and G are the bulk modulus and the shear modulus, respectively, and $\Delta z_{\min}$ is the smallest dimension of an adjacent zone in the normal direction [17–27,31].

Noting that all of the analyses presented in this study are quasi-static. In other words, the seismic wave propagation in the soil and its impacts on the tunnels were not considered. To model the fault displacement, a boundary velocity was setup in a given number of calculation steps. If the applied maximum displacement is equal to d value, then the number of steps (N) will be equal to $N = d/V$, where V is the velocity [31]. The direction of the given velocities, specified in Fig. 1 (according to the fault type), are parallel to the fault plane.

The tunnel supporting system, i.e., a shotcrete layer was simulated by liner elements. According to the FLAC3D user manual, these structural elements have the linear-elastic behavior [31], and therefore; unlike the studies conducted in Refs. [32–44], damages and instability of structural elements cannot be expected. The Liner elements are attached to the zone by links, and hence; a shear-directed frictional interaction occurs between the liner and grids. The liner-zone interface stiffness (normal stiffness (K_n) and shear stiffness (K_s)) was chosen one hundred times of the equivalent stiffness of Eq. (1) [31].

The finite difference running procedure consists of three steps.

1) The first step of the finite difference process includes

setting up of the numerical model, and assigning the boundary condition and the initial stresses (taking into account of the gravity) [45,46]. In FLAC3D, two types of boundary are used for a simulation: real and artificial. Real boundaries are those exist in the physical object being modeled (e.g., tunnel surface) while artificial boundaries do not exist in the reality [31]. For assigning and satisfying the boundary condition, either of two methods of fixed or stress boundary can be used. In this study, the boundary nodes on all sides of the model were fixed in the directions perpendicular to the *Y*-*Z* plane and to the *X*-*Z* plane, while the nodes at the base of the model were fixed in the vertical direction.

On the other hand, the mesh sizes were refined around the tunnel, and zone sizes were set to be small in the foot wall close to the fault plane.

2) In the second step, the tunnel was excavated, the shotcrete was installed, and the system was brought to the equilibrium. Then, displacements and velocities were set to zero.

3) In the third step, the velocities were specified to the boundaries of the hanging wall to shift it in the fault direction. The large strain mode was used for this step, and the nodal coordinates were then updated at each calculation step.

In Fig. 2, the *W* parameter is introduced as the horizontal distance from the bedrock fault to the location of the surface outcropping, i.e., the location where the ground displacement is equal to zero.

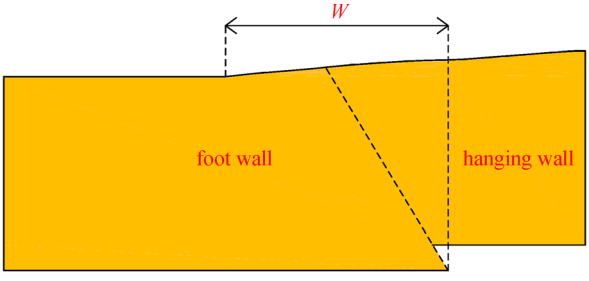

Fig. 2 Definition of *W* parameter.

In FLAC3D, at each stage of an analysis, the maximum unbalanced force in the model should be monitored. When the ratio of the maximum unbalanced force magnitude for all the grid points divided by the average applied mechanical force magnitude is smaller than 1×10^{-5}, it can be assumed that the model is in the equilibrium [31].

2.2 Verification of finite difference model

First of all, the centrifuge physical test conducted by Kiani [16] is introduced. Because, it was contributed to calibrate the accuracy of predictions by the numerical simulation. Kiani [16] investigated the effects of reverse and normal faulting on a segmental tunnel. In the tests, the dry sand was poured in the rigid box in layers and then compacted. After reaching the desired soil thickness, the segmental tunnel (constructed by asbestos cement pipes) was placed in the soil layer. Then, the filling was continued until the soil reached to the ground level. The properties of the soil and the tunnel in the physical model are summarized in Table 1.

Table 1 Properties of the soil and of the tunnel in the centrifuge test level [16]

parameter	unit	value
elastic modulus of soil	MPa	20
friction angle of soil	–	37
soil density	kg/m^3	1630
Poisson's ratio of soil	–	0.3
cohesion of soil	kN/m^2	0
segment density	kg/m^3	2600
Poisson's ratio of segment	–	0.28
elastic modulus of segment	GPa	20

The centrifuge acceleration set to 50*g*, and the fault displacement (in the fault direction) was applied to the moving part of the box. The tunnel displacements and the tunnel affected length due to the reverse and normal faulting are presented in Table 2.

The dimensions of numerical model were chosen 50 times greater than the physical model tests. Then, sensitive analyses for the boundaries location as well as the mesh size were performed to check their effects on the results. For various mesh refinements, tunnel deflection values (i.e., vertical displacement) due to the normal faulting are shown in Fig. 3. As seen, the results are not mesh dependent and the difference between the results are less than 1%. On the other hand, an unstructured discretization

Table 2 The displacement of tunnel obtained by the centrifuge physical test model level [16]

fault type	fault angle	height of overburden of soil (m)	the length of the tunnel affected by normal fault movement (m)	maximum displacement of tunnel (m)
reverse	60°	4.42	–	0.550
reverse	75°	4.42	–	0.256
normal	60°	4.42	9.44	2.500
normal	75°	5.90	11.5	2.500

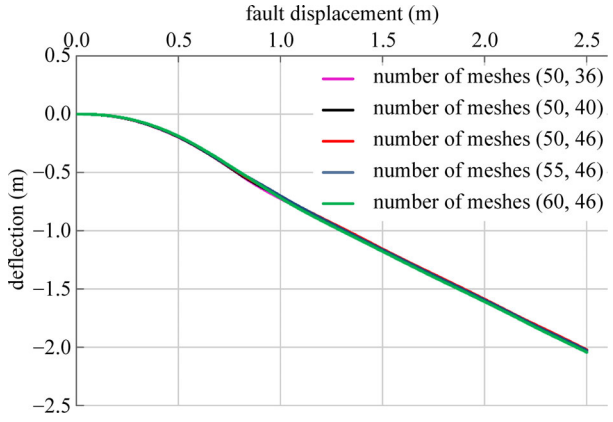

Fig. 3 Effect of mesh sizes on the tunnel deflection values (the first and second numbers in the legend of figure represent the number of meshes in the *Y* and *Z* directions, respectively).

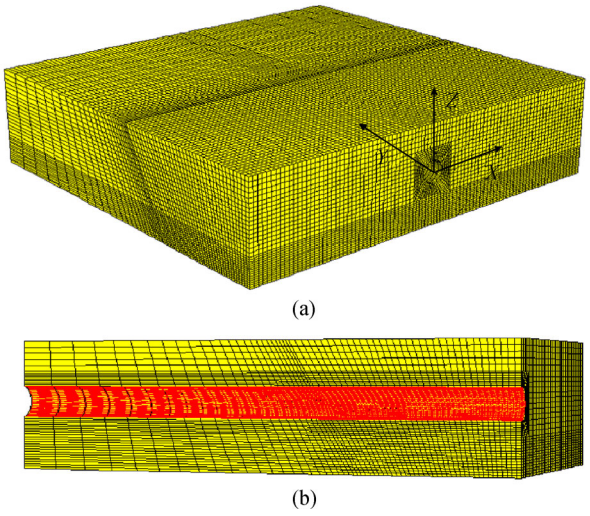

Fig. 4 Perspective view of the model and its meshes: (a) general model; (b) half of model along the tunnel axis.

of the elements particularly below tunnel are generated on the basis of FLAC3D tutorial advisement to avoid undesirable effects. The numerical model dimensions presented in Fig. 4 are 112 m wide (*X* direction), 100 m long (*Y* direction, tunnel axis direction), and 25 m high (*Z* direction) consisting of 219840 zones and 229665 grid points.

As specified in Section 2.1, the velocities were applied to the boundaries of the hanging wall in *N* steps to reach the required displacement. Considering the model dimensions (shown in Fig. 4), and assuming the Mohr-Coulomb failure criterion with appropriate stress-strain law (see Section 3), the number of steps was chosen as a value so that the results of the finite difference analysis met those of the experimental one. That is, for the reverse and normal faulting, the numbers of steps were respectively set 3500 and 15000 which imply a velocity $V = 7.1\times\ 10^{-4}$ and $V = 1.67 \times 10^{-4}$ (m/calculation steps) in order to give the movement of 2.5 m in the direction of the faults. By this process, the results of the finite difference method were in a good agreement with the results of the centrifuge physical model, i.e., the maximum displacement of the tunnel in the various conditions (mentioned in Table 2) was very similar to that obtained by numerical procedure.

3 Parametric study and discussion

The parametric study consists of numerous investigations to evaluate the effects of various parameters such as the soil geo-mechanical properties, the support system properties, the tunnel depth, and the fault dip angle on outputs of fault movements including the development of soil plastic strains, the tunnel displacements, and the ground settlements along the tunnel longitudinal axis. In the analyses, two different relative densities were considered for the dry soil.

1) A dense soil with the strain-hardening/softening constitutive model implemented in FLAC3D. This model allows representation of nonlinear material softening and hardening behavior based on prescribed variations of the Mohr-Coulomb model properties (i.e., cohesion, friction, dilation, and tensile strength) as functions of the deviatoric plastic strain. The friction and dilation angles were assumed to decrease linearly with the increase of deviatoric plastic strains up to 10% (Fig. 5) [47].

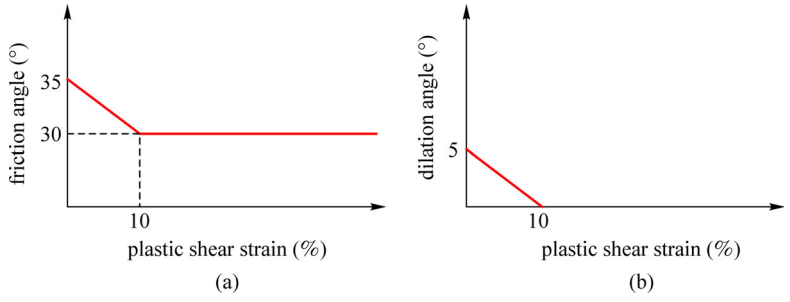

Fig. 5 (a) Friction and (b) dilation angle parameters versus plastic shear strain used for the dense soil.

2) A loose soil characterized by the linear elastic-perfectly plastic constitutive model with the Mohr-Coulomb shearing criterion implemented in FLAC3D. In this case, the strength parameters remain constant after failure.

The basic properties of the dense and loose granular soils, and the support system are summarized in Tables 3 and 4, respectively. As seen, each of the soil properties is introduced by a deterministic value. In fact, soil properties can vary from a point to another point even in uniform deposits. Therefore, statistical distributions such as the Normal and Log-Normal distributions are required to describe soil properties, and stochastic approaches are necessary to analyze the problem. This method of analyses gives better engineering judgment of such as the work available in Refs. [48–50]. But for a preliminary study, a deterministic analysis in which the mean values of parameters are used is sufficient.

Table 3 Properties of the soil [51,52]

parameter	unit	dense soil	loose soil
elastic modulus	MPa	34	15
peak friction angle	–	34	30
peak dilation angle	–	4 [a)]	0
residual friction angle	–	30	30
residual dilation angle	–	0 [a)]	0
density	kg/m^3	1800 [b)]	1500 [b)]
Poisson's ratio	–	0.3	0.3
cohesion	kN/m^2	0	0

Note: a) The dilation angle is assumed to be equal to $\phi = \varphi - 30$ where φ is the friction angle; b) assumed by authors.

Table 4 Properties of the shotcrete

parameter	unit	value
density	kg/m^3	2600
Poisson's ratio	–	0.28
thickness	m	0.3
elastic modulus	GPa	34

3.1 Effects of the shotcrete thickness

Three values of 0.25, 0.30, and 0.35 m are considered for the shotcrete thickness while the other parameters remain constant. For the reverse faulting, it can be observed from Fig. 6, once the shotcrete thickness is increased, the plastic strains around the tunnel tends to spread out over a wider zone on the hanging wall but they are reduced on the foot wall. This is because, a higher rigidity of the shotcrete layer prevents it from moving, and therefore; the relative displacement between the soil and the surrounded shotcrete is increased (meaning soil shearing). In the normal faulting cases, the results are inverse but with less intensity (see Fig. 7).

The longitudinal displacement profiles of ground surface are shown in Fig. 8. As observed, independent of the shotcrete thickness, the W values are respectively 28 and 30 m for the reverse and normal faulting (the soil layer thickness in all of the tests is equal to 25 m). The ground surface as well as the tunnel crown is more influenced by the normal faulting rather than by the reverse one.

Figure 8 also shows that increasing of the shotcrete thickness slightly reduces the ground surface displacements for the reverse faulting. Meanwhile, it has almost no

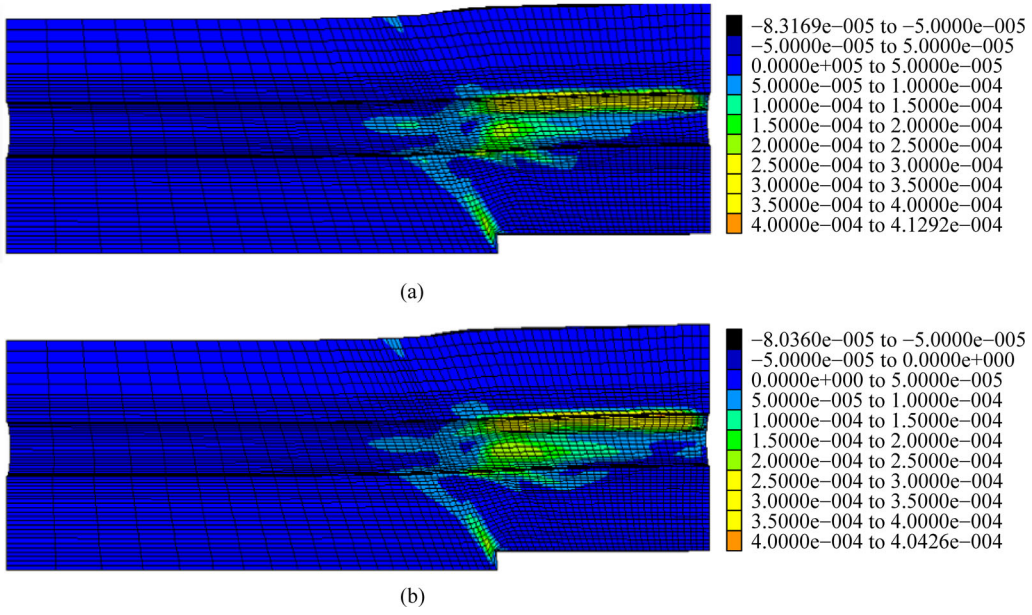

Fig. 6 Effect of the tunnel shotcrete thickness on the deformed mesh due to the reverse faulting (the properties of the dense soil are mentioned in Table 3). (a) Shotcrete thickness = 0.30 m; (b) shotcrete thickness = 0.35 m.

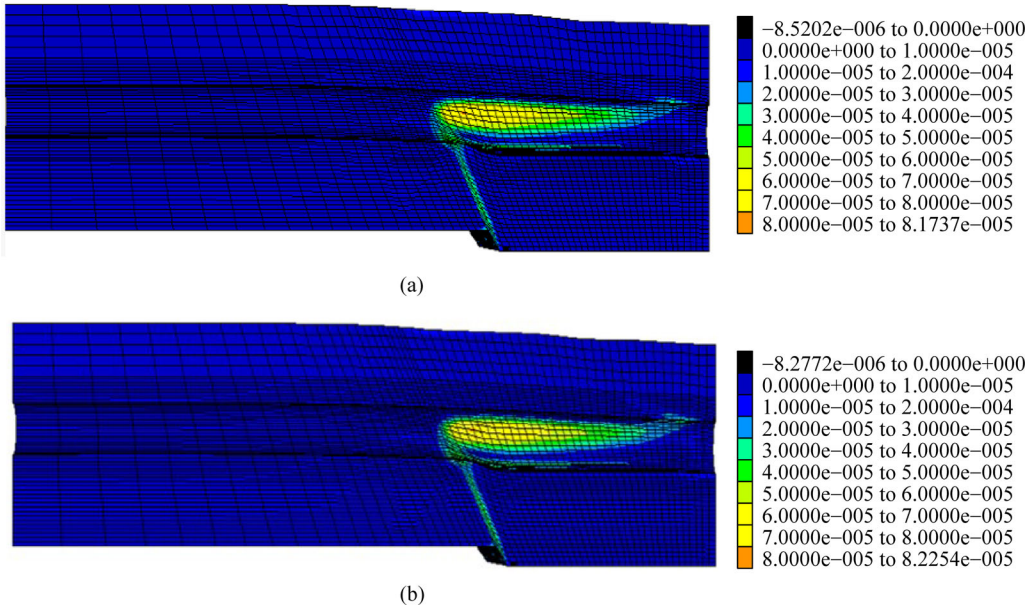

Fig. 7 Effect of the tunnel shotcrete thickness on the deformed mesh due to the normal faulting (the properties of the dense soil are mentioned in Table 3). (a) Shotcrete thickness = 0.30 m; (b) shotcrete thickness = 0.35 m.

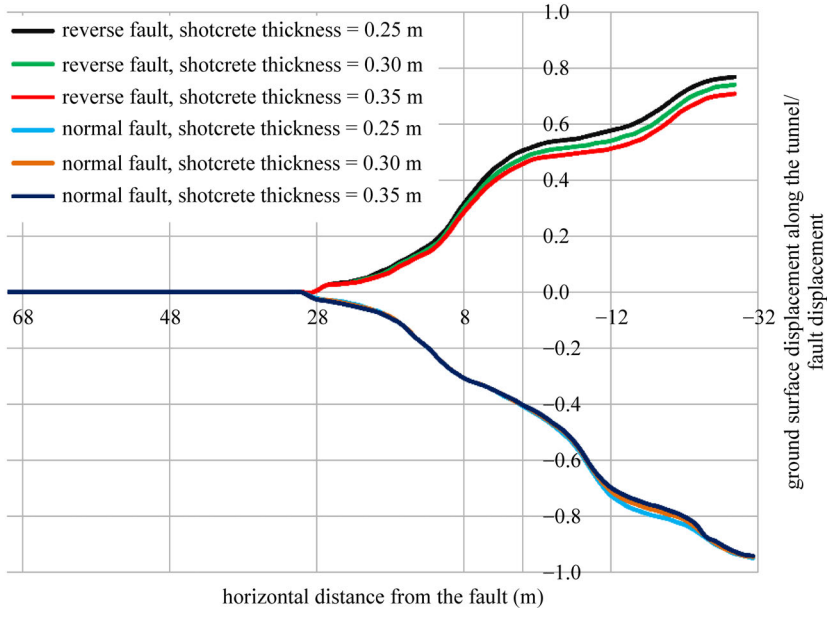

Fig. 8 Effect of shotcrete thickness on the settlement profile along the tunnel crossing a reverse fault or a normal fault.

effect in the case of a normal faulting. This result can be cautiously extended to the maximum tunnel displacement but with more intensity compared to the ground surface displacement (Fig. 9). Increasing of the shotcrete thickness linearly reduces the maximum tunnel displacement. On the other hand, like for the ground surface, the tunnel vertical deformation is greater while crossing normal faults.

3.2 Effects of the mechanical properties of soil

Each of following different soils (i.e., gravel, sandy gravel with few fines, and uniform fine sand with properties available in Table 5) was solely considered around tunnel to evaluate the effects on the outputs. Comparing the input data of the first case of Fig. 6 and the first case of Fig. 10, it

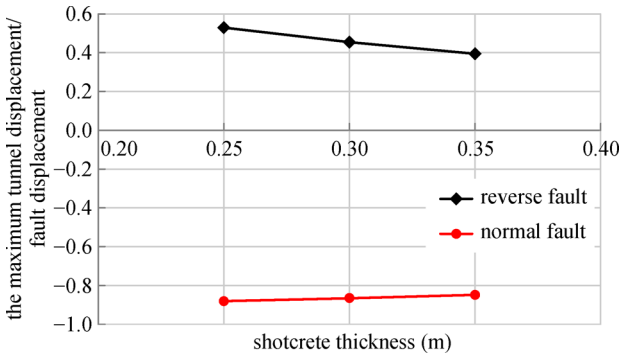

Fig. 9 Effect of the shotcrete thickness on the maximum vertical displacement of a tunnel crossing a reverse fault or a normal fault.

can be concluded that a greater friction angle results in a smaller deformed zone. Similarly, comparing the input data of the first and the second cases of Fig. 10 shows that the maximum value of plastic strains contours increases once the soil stiffness becomes greater. The reduction of the plastic zone extension in the first case can be associated to the increase of the friction angle.

In the soil with greater geo-mechanical properties, the extent of deformed meshes around the tunnel is spread out over a wider zone in the hanging wall side of normal faulting and the maximum plastic strain is greater, as well (Fig. 11). As well, comparing Figs. 10 and 11, it can be found that the probable failure zone of soil is closer to the fault plane for the normal faulting.

Figure 12 implies, unlike for the normal faulting, the soil geo-mechanical properties have an inverse relation to the absolute vertical settlement for the case of a reverse fault. Considering the input data in Table 5, the major difference between the results of the loose and dense soils refers to the elastic modulus of soil as well as the soil density. A negligible difference among the results of various loose (or dense) soils is associated to the soil friction angle. On the other hand, in the normal faulting, while the soil properties

Table 5 Effect of the soil geo-mechanical properties on the maximum tunnel vertical displacement in the reverse and normal faulting

peak friction angle (°)	peak dilation angle (°)	soil density (kg/m^3)	elastic modulus of soil (MPa)	maximum vertical tunnel displacement for reverse faulting (m)	maximum vertical tunnel displacement for normal faulting (m)
34	4	1800	34	1.14	2.16
36	6	1800	34	1.17	2.16
38	8	1800	34	1.19	2.16
30	–	1500	15	0.62	2.18
28	–	1500	15	0.59	2.18
24	–	1500	15	0.54	2.18

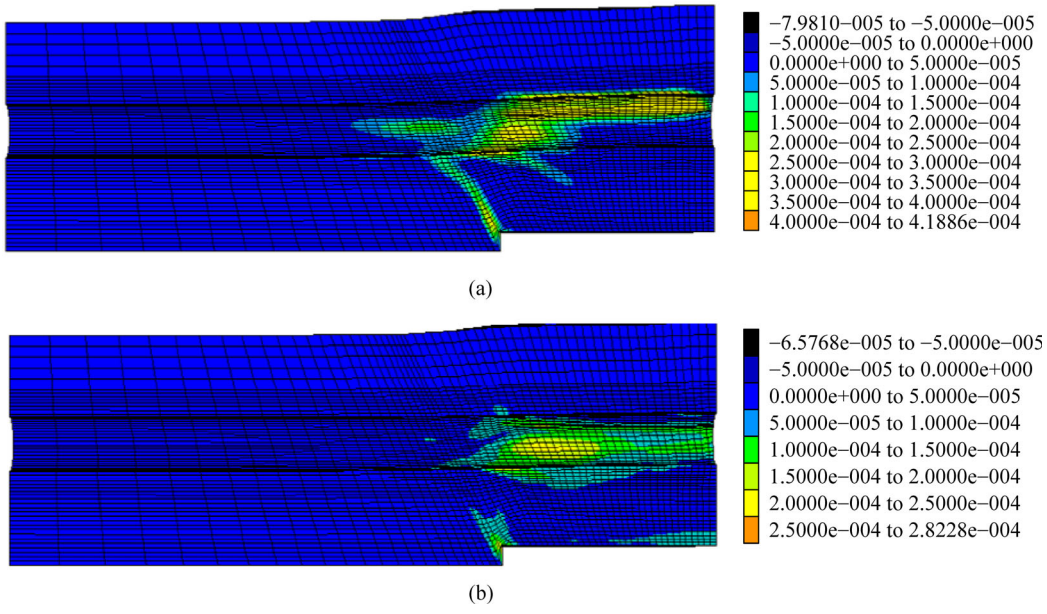

Fig. 10 Effect of the soil mechanical properties on the deformed mesh due to the reverse faulting. (a) φ= 38°, ψ= 8°, soil density = 1800 kg/m^3, elastic modulus of soil = 24 MPa; (b) φ= 30°, ψ= 0°, soil density = 1500 kg/m^3, elastic modulus of soil = 15 MPa.

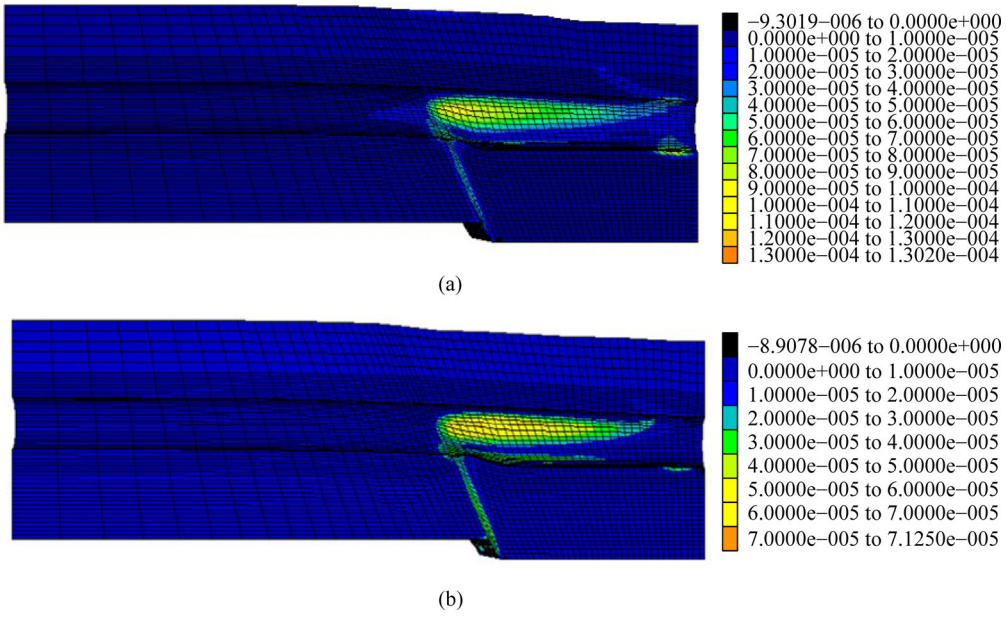

Fig. 11 Effect of the soil mechanical properties on the deformed mesh due to the normal faulting. (a) φ= 38°, ψ= 8°, soil density = 1800 kg/m^3, elastic modulus of soil = 24 MPa; (b) φ= 30°, ψ= 0°, soil density = 1500 kg/m^3, elastic modulus of soil = 15 MPa.

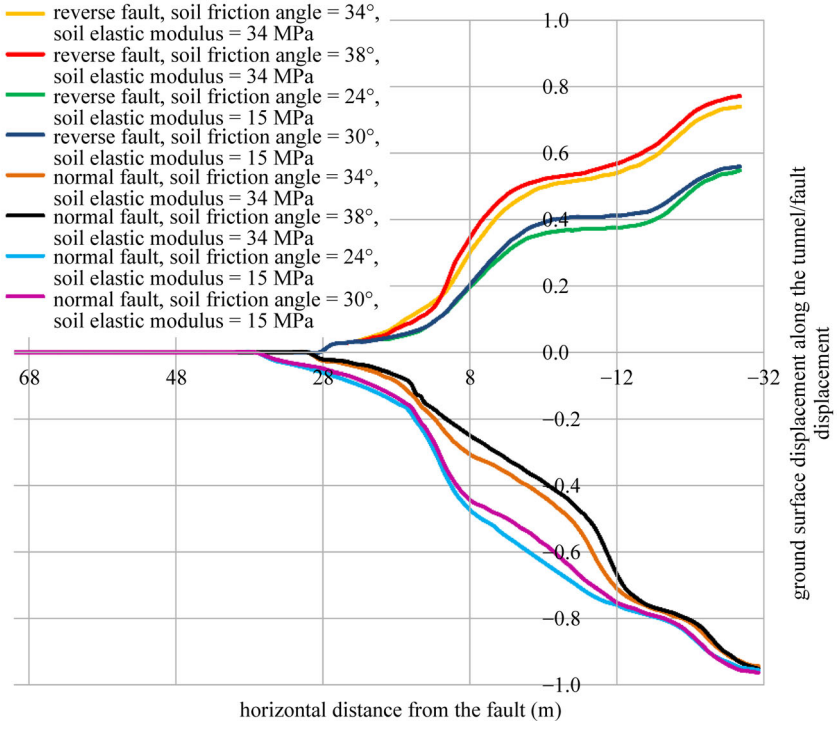

Fig. 12 Effect of the soil geo-mechanical properties on the settlement profile along the tunnel crossing a reverse fault or a normal fault.

have almost no effect on the maximum settlement, the settlement profiles are greatly influenced when the soil geo-mechanical properties are changed. As well, the W value of the loose sand is different from that of the dense sand.

It seems that when the tectonic forces are compressive and produce a reverse faulting, a part of the total force tends to compress the soil in order to make it denser. In this case, the loose soil which has the low elasticity modulus quickly deforms, and then a lower part of the total force remains to move the tunnel. In other words, a part of total amount of compressive force leads the soil particles to

move to make the soil mass denser.

Unlike for the reverse faulting cases (Fig. 12), the W value in the normal faulting is dependent upon the soil geo-mechanical properties, and it becomes greater for the loose soil.

In this section, the Elasticity modulus of shotcrete layer is selected as a constant value; hence, the output results also reflects the effect of the relative elasticity modulus of the shotcrete to the soil.

3.3 Effects of the tunnel depth

One of the parameters that can have a significant influence on the performance of the tunnel is depth. The tunnel depths are varied from 11.8 to 7.4 and to 14 m in order to investigate the influence of the overburden on the development of the shear plastic zone as well as on the settlements, and on the tunnel crown at the final stage of the faulting. It can be inferred from Fig. 13 that once the overburden above tunnel is smaller, its resistance against an upward movement is lower. For the normal faulting, as shown in Fig. 14, when the tunnel is located at the lower depth, the maximum plastic strain is bigger, and simultaneously; a greater part of the soil around the tunnel is effected by the fault movement.

The maximum plastic deformations are localized at the tunnel crown for the cases of reverse faulting and at the tunnel center levels for the cases of normal faulting.

Figure 15 shows that when the tunnel is located close to the ground surface, the displacements of the ground surface are reduced in the hanging wall side. As well, the settlements tend to have a uniform trend over the influenced area. As seen in Fig. 16, for both reverse faulting and normal faulting, deeper tunnels are imposed to a greater maximum displacements.

3.4 Effects of the fault dip angle

Here, the fault dip angle is increased from 60° to 90° with an increment of 15°. As observed in Fig. 17, the maximum plastic strain increases on the hanging wall while it is reduced on the foot wall when the reverse faulting dip angle becomes smaller. However, more amount of zones become plastic as the dip angle is lower. That is, when the dip angle is equal to 90°, less zones deforms compared to the smaller dip angle. As well, in the normal faulting, less zones deforms when the dip angle becomes greater (Fig. 18).

Figure 19 shows that for both the reverse and normal faulting, a greater fault dip angle leads to smaller settlements and the W value. Therefore, the lower displacements and probably the least damage can be expected for structures when the fault dip angle is about 90°. However, it seems that it is not very effective for the lower fault dip angles, i.e., between 60° and 75°.

The results of parametric study also indicate that in the case of the reverse faulting, increasing the fault angle causes the maximum tunnel displacement to reduce (Fig. 20).

3.5 Fault movement and safety of surface and buried structures

In addition to the maximum displacements value of ground surface as well as the tunnel crown, the corresponding gradients are also critical factors, and must be considered

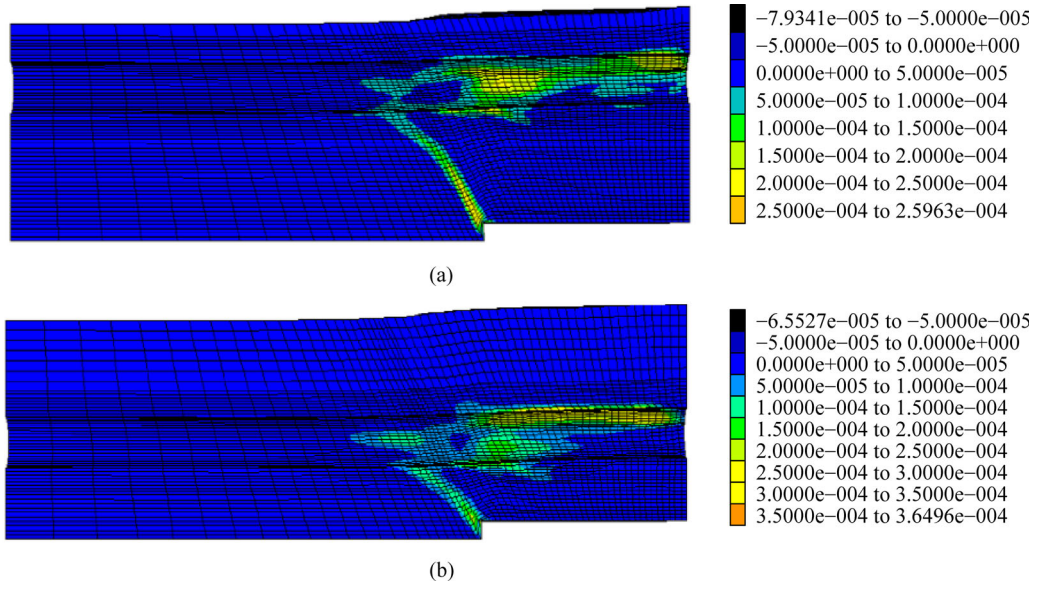

Fig. 13 Effect of the tunnel depth on the deformed mesh due to the reverse faulting. (a) Tunnel depth = 7.4 m; (b) tunnel depth = 14 m.

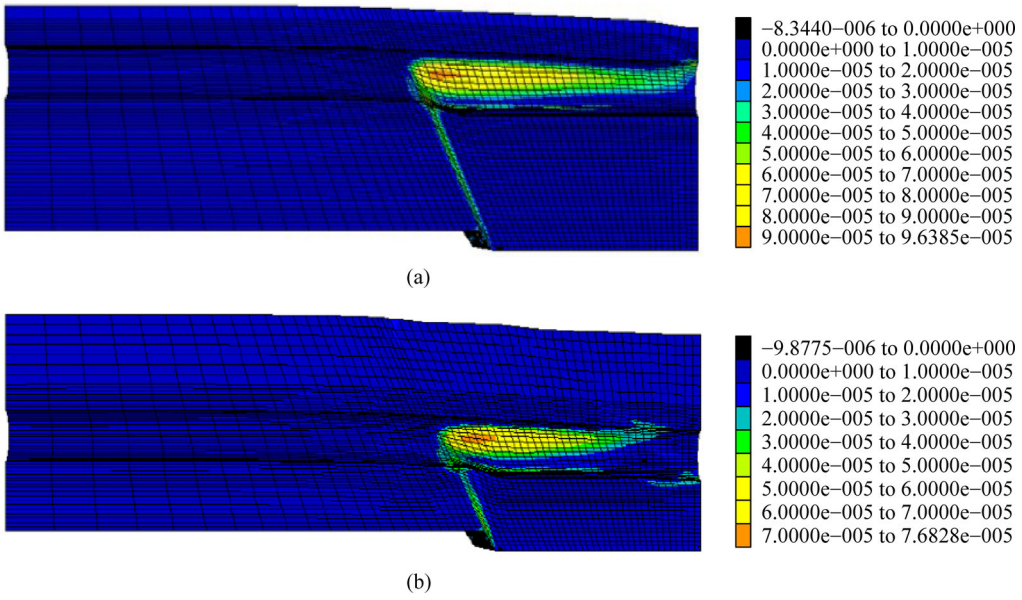

Fig. 14 Effect of the tunnel depth on the deformed mesh due to the normal faulting. (a) Tunnel depth = 7.4 m; (b) tunnel depth = 14 m.

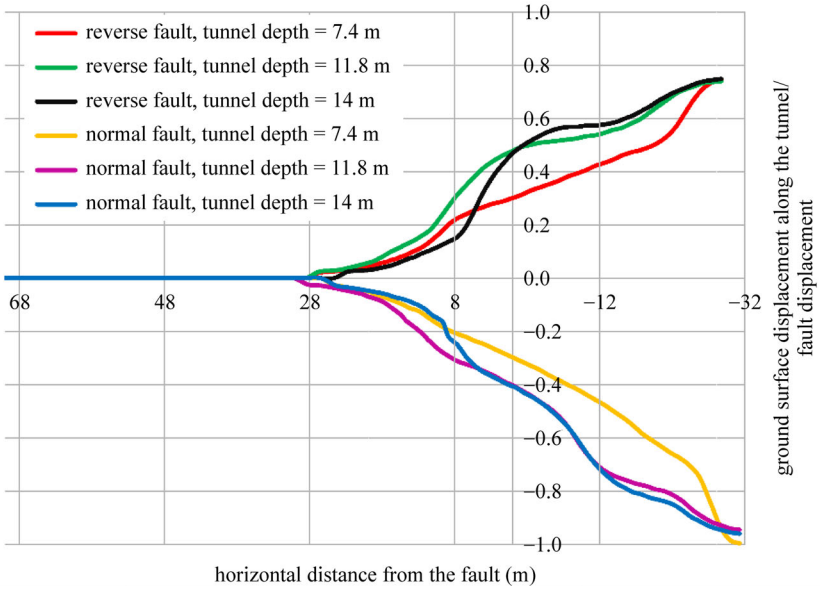

Fig. 15 Effect of the tunnel depth on the settlement profile along the tunnel crossing a reverse fault or a normal fault.

in the design. Table 6 represents the value of maximum gradient and their corresponding location (measured from the bedrock fault). For the reverse fault, the weaker soil gives the smaller values while the shotcrete thickness and fault dip angle have almost no effect. In more or less all the tests, for the case of the normal faulting, the value of the maximum gradient of settlement is higher than the one due to the reverse faulting.

Table 7 gives the tunnel structure deformation due to the reverse fault movement. Obviously, the shotcrete thickness is the most effective parameter for the deformation control. On the other hand, a weaker soil with a smaller dip fault angle will induce the lower damage to tunnels.

4 Conclusions

In this paper, by the three dimensional numerical simulation, the problem of a reverse fault or normal fault movements on a crossing shotcrete tunnel is studied. The parametric study investigates the effects of soil properties, the tunnel and its support properties, and spatial location of

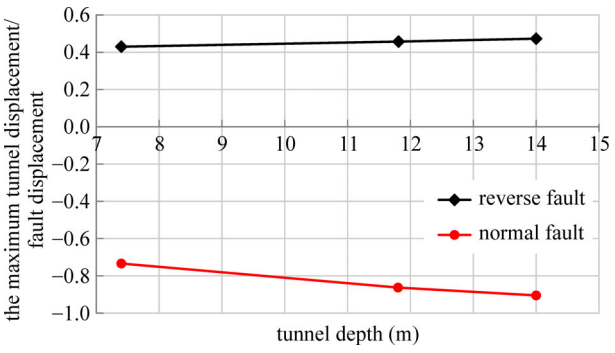

Fig. 16 Effect of the tunnel depth on the maximum displacement of a tunnel crossing a reverse fault or a normal fault.

fault plane on the interaction between the tunnel and its medium. It qualitatively finds out their influences on the amount of the deformed zone, on the tunnel maximum displacement, and on the ground surface settlements along the tunnel axis. The distinguished results are as follows.

1) Unlike the fault dip angle and the soil friction angle, the parameters including the tunnel support rigidity, the soil stiffness, and the tunnel depth have a direct relation to the value of developed plastic strains in the hanging wall side when a reverse faulting occurs.

2) The influenced length of the ground surface along the tunnel axis due to the fault movement is independent of both the tunnel support rigidity and the soil stiffness. But

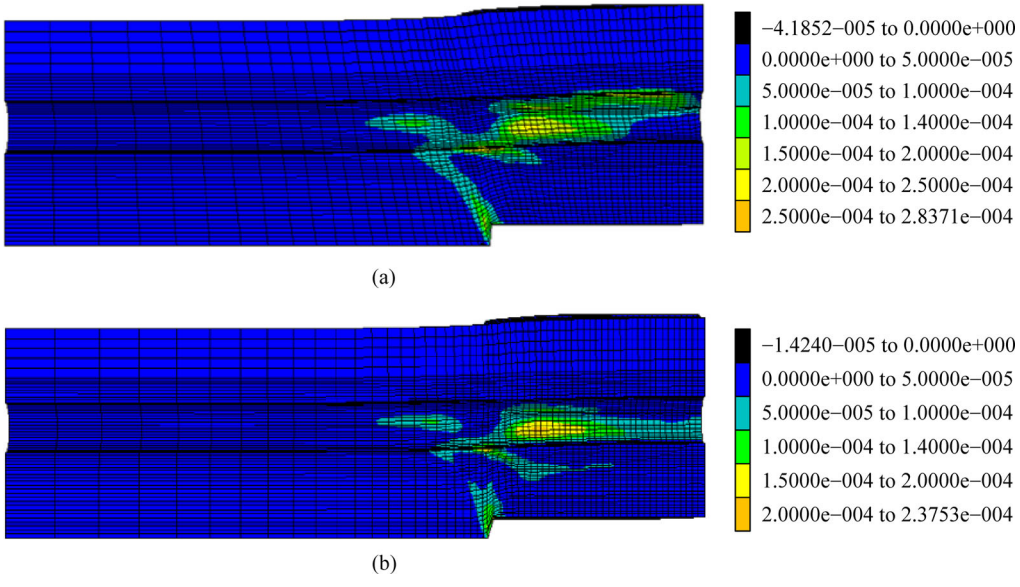

Fig. 17 Effect of the reverse fault dip angle on the deformed mesh. (a) Fault dip angle = 75°; (b) fault dip angle = 90°.

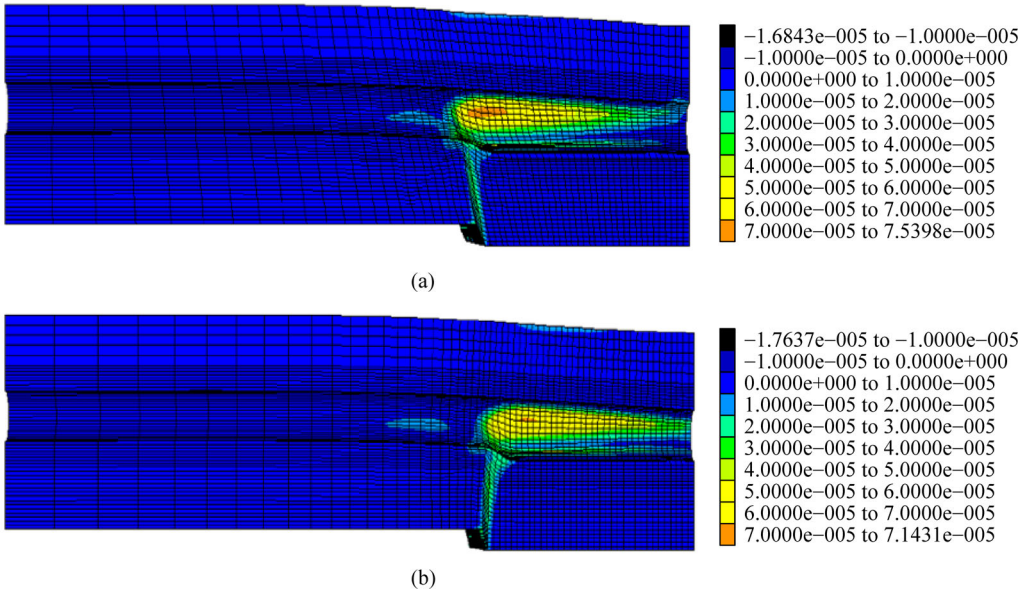

Fig. 18 Effect of the normal fault dip angle on the deformed mesh. (a) Fault dip angle = 75°; (b) fault dip angle = 90°.

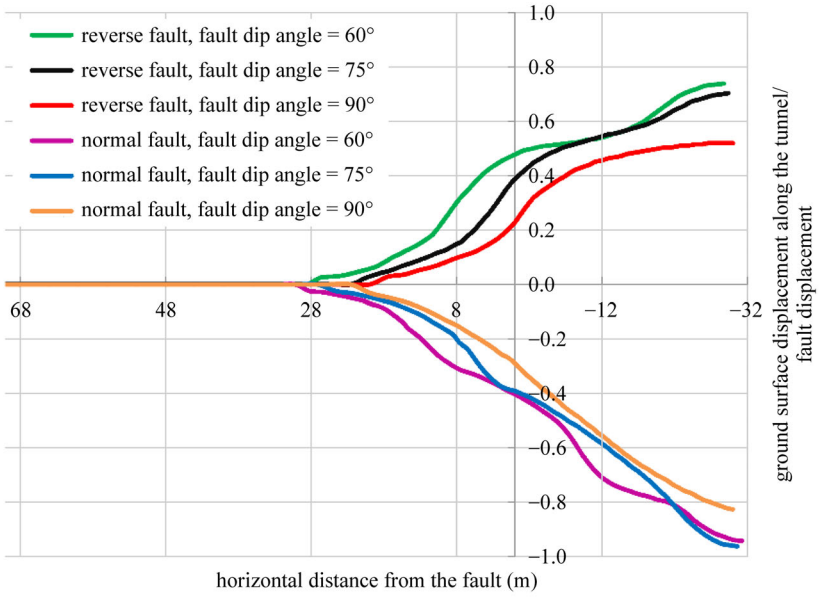

Fig. 19 Effect of the fault dip angle on the settlement profile along the tunnel crossing a reverse fault or a normal fault.

Table 6 The maximum gradient of settlement and corresponding location for the different cases (reverse and normal faults)

the cases	point of the maximum gradient in the reverse fault (m) Y	maximum gradient in the reverse fault	point of the maximum gradient in the normal fault (m) Y	maximum gradient in the normal fault
the base example case	8	−0.09	−9	0.10
shotcrete thickness = 0.25 m	8	−0.10	−9	0.10
shotcrete thickness = 0.35 m	8	−0.09	−9	0.10
dense sand, ϕ = 36°, E_s = 24 MPa	8	−0.11	−10	0.11
dense sand, ϕ = 38°, E_s = 24 MPa	10	−0.14	−12	0.12
loose sand, ϕ = 30°, E_s = 15 MPa	10	−0.07	11	0.12
loose sand, ϕ = 28°, E_s = 15 MPa	7	−0.065	11	0.12
loose sand, ϕ = 24°, E_s = 15 MPa	10	−0.06	11	0.12
tunnel depth = 7.4 m	−15	−0.10	−28	0.16
tunnel depth = 14 m	5	−0.14	8	0.18
fault dip angle = 75°	2	−0.09	5	0.09
fault dip angle = 90°	−2	−0.09	0	0.06

Note: The base example input data are: shotcrete thickness = 0.30 m, dense sand, ϕ= 34°, E_s (elasticity modulus of soil) = 24 MPa, tunnel depth = 11.8 m, and fault dip angle = 60°.

certainly, this parameter is smaller when the fault dip angle is greater.

3) In the reverse faulting, while the friction angle has a negligible effect, the soil stiffness has remarkable influence on the settlement profile (and its gradient) and on the tunnel crown displacement (and its deformation). On the other hand, in the normal faulting, the soil properties have almost no effect on the maximum settlement, but greatly on the settlement profile. The location of the higher gradient moves to the hanging wall as the soil becomes stiffer.

4) The greater displacements of the ground surface and the tunnel crown can be seen for the deeper tunnels in the hanging wall side for any form of faulting.

5) The fault dip angle is the other parameter that seems important for the safety design. When the angle between the fault and tunnel axis is 90 °, smaller displacements are imposed to the ground surface and to the tunnel crown. As well, the tunnel support rigidity is the most effective parameter in controlling the deformations.

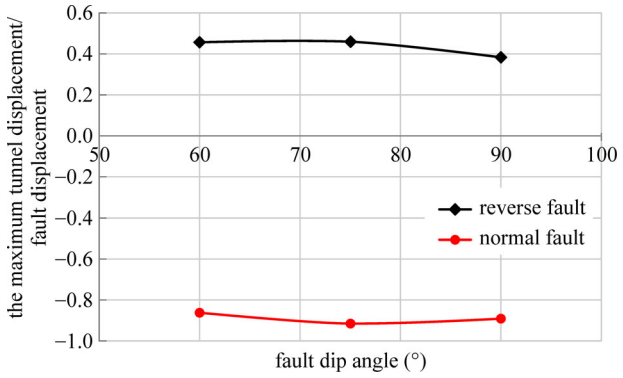

Fig. 20 Effect of the fault dip angle on the maximum displacement of a tunnel crossing a reverse fault or a normal fault.

Table 7 Tunnel deformation in the horizontal and vertical directions in the reverse fault movement

the cases	tunnel deformation in the horizontal direction (%)	tunnel deformation in the vertical direction (%)
the base example case	1.64	1.66
shotcrete thickness = 0.25 m	2.91	2.96
shotcrete thickness = 0.35 m	0.86	0.91
dense sand, ϕ = 36°, E_s = 24 MPa	1.56	1.59
dense sand, ϕ = 38°, E_s = 24 MPa	1.50	1.54
loose sand, ϕ = 30°, E_s = 15 MPa	1.40	1.44
loose sand, ϕ = 28°, E_s = 15 MPa	1.33	1.35
loose sand, ϕ = 24°, E_s = 15 MPa	1.18	1.18
tunnel depth = 7.4 m	1.74	1.74
tunnel depth = 14 m	1.79	1.88
fault dip angle = 75°	2.20	2.20
fault dip angle = 90°	2.40	2.44

Note: The base example input data are: shotcrete thickness = 0.30 m, dense sand, ϕ = 34°, E_s (elasticity modulus of soil) = 24 MPa, tunnel depth = 11.8 m, and fault dip angle = 60°.

References

1. Baziar M H, Nabizadeh A, Lee C J, Hung W Y. Centrifuge modeling of interaction between reverse faulting and tunnel. Soil Dynamics and Earthquake Engineering, 2014, 65: 151–164
2. Baziar M H, Nabizadeh A, Mehrabi R, Lee C J, Hung W Y. Evaluation of underground tunnel response to reverse fault rupture using numerical approach. Soil Dynamics and Earthquake Engineering, 2016, 83: 1–17
3. Kiani M, Akhlaghi T, Ghalandarzadeh A. Experimental modeling of segmental shallow tunnels in alluvial affected by normal faults. Tunnelling and Underground Space Technology, 2016, 51: 108–119
4. Lin M L, Chung C F, Jeng F S, Yao T C. The deformation of overburden soil induced by thrust faulting and its impact on underground tunnels. Engineering Geology, 2007, 92(3–4): 110–132
5. Wang Z, Zhang Z, Gao B. Seismic behavior of the tunnel across active fault. In: The 15th World Conference on Earthquake Engineering. Lisbon, 2012
6. Lin M L, Chung C F, Jeng F S. Deformation of overburden soil induced by thrust fault slip. Engineering Geology, 2006, 88(1–2): 70–89
7. Loukidis D, Bouckovalas G D, Papadimitriou A G. Analysis of fault rupture propagation through uniform soil cover. Soil Dynamics and Earthquake Engineering, 2009, 29(11–12): 1389–1404
8. Mortazavi Zanjani M, Soroush A. Numerical modelling of fault rupture propagation through layered sands. European Journal of Environmental and Civil Engineering, 2017, 23(9): 1139–1155
9. Hazeghian M, Soroush A. DEM simulations to study the effects of the ground surface geometry on dip-slip faulting through granular soils. European Journal of Environmental and Civil Engineering, 2020, 24(7): 861–879
10. Anastasopoulos I, Callerio A, Bransby M F, Davies M C R, Nahas A E, Faccioli E, Gazetas G, Masella A, Paolucci R, Pecker A, Rossignol E. Numerical analyses of fault-foundation interaction. Bulletin of Earthquake Engineering, 2008, 6(4): 645–675
11. Anastasopoulos I, Gazetas G. Foundation-structure systems over a rupturing normal fault: Part II. Analysis of the Kocaeli case histories. Bulletin of Earthquake Engineering, 2007, 5(3): 277–301
12. Bransby M, Davies M, El Nahas A, Nagaoka S. Centrifuge modelling of reverse fault-foundation interaction. Bulletin of Earthquake Engineering, 2008, 6(4): 607–628
13. Bransby M, Davies M, Nahas A E. Centrifuge modelling of normal fault-foundation interaction. Bulletin of Earthquake Engineering, 2008, 6(4): 585–605
14. Ng C W W, Soomro M A, Hong Y. Three-dimensional centrifuge modelling of pile group responses to side-by-side twin tunnelling. Tunnelling and Underground Space Technology, 2014, 43: 350–361
15. Soomro M A, Ng C W W, Liu K, Memon N A. Pile responses to side-by-side twin tunnelling in stiff clay: Effects of different tunnel depths relative to pile. Computers and Geotechnics, 2017, 84: 101–116
16. Kiani M. Effects of Surface Fault Rupture on Shallow Segmental Soil Tunnels-Centrifuge Modeling. Tabriz: University of Tabriz, 2016 (in Persian)
17. Do N A, Dias D. A comparison of 2D and 3D numerical simulations of tunnelling in soft soils. Environmental Earth Sciences, 2017, 76(3): 102
18. Do N A, Dias D, Oreste P. 2D seismic numerical analysis of segmental tunnel lining behaviour. Bulletin of the New Zealand Society for Earthquake Engineering, 2014, 47(3): 206–216
19. Do N A, Dias D, Oreste P. Numerical investigation of segmental tunnel linings-comparison between the hyperstatic reaction method and a 3D numerical model. Geomechanics and Engineering, 2018, 14(3): 293–299

20. Do N A, Dias D, Oreste P, Djeran-Maigre I. 2D numerical investigations of twin tunnel interaction. Geomechanics & Engineering, 2014, 6(3): 263–275
21. Do N A, Dias D, Oreste P, Djeran-Maigre I. The behaviour of the segmental tunnel lining studied by the hyperstatic reaction method. European Journal of Environmental and Civil Engineering. 2014, 18(4): 489–510
22. Do N A, Dias D, Oreste P. 3D numerical investigation on the interaction between mechanized twin tunnels in soft ground. Environmental Earth Sciences, 2015, 73(5): 2101–2113
23. Do N A, Dias D, Oreste P, Djeran-Maigre I. 2D numerical investigation of segmental tunnel lining behavior. Tunnelling and Underground Space Technology, 2013, 37: 115–127
24. Do N A, Dias D, Oreste P, Djeran-Maigre I. 2D tunnel numerical investigation: The influence of the simplified excavation method on tunnel behaviour. Geotechnical and Geological Engineering, 2014, 32(1): 43–58
25. Do N A, Dias D, Oreste P, Djeran-Maigre I. Three-dimensional numerical simulation for mechanized tunnelling in soft ground: The influence of the joint pattern. Acta Geotechnica, 2014, 9(4): 673–694
26. Do N A, Dias D, Oreste P, Djeran-Maigre I. Three-dimensional numerical simulation of a mechanized twin tunnels in soft ground. Tunnelling and Underground Space Technology, 2014, 42: 40–51
27. Do N A, Dias D, Oreste P, Djeran-Maigre I. Behaviour of segmental tunnel linings under seismic loads studied with the hyperstatic reaction method. Soil Dynamics and Earthquake Engineering, 2015, 79: 108–117
28. Rabczuk T, Ren H, Zhuang X. A nonlocal operator method for partial differential equations with application to electromagnetic waveguide problem. Computers, Materials & Continua, 2019, 59(1): 31–35
29. Guo H, Zhuang X, Rabczuk T. A deep collocation method for the bending analysis of Kirchhoff plate. Computers, Materials & Continua, 2019, 59(2): 433–456
30. Anitescu C, Atroshchenko E, Alajlan N, Rabczuk T. Artificial neural network methods for the solution of second order boundary value problems. Computers, Materials & Continua, 2019, 59(1): 345–359
31. Itasca. Fast Lagrangian Analysis of Continua in 3-Dimension (FLAC3D V3.1). Itasca Consulting Group, 2007
32. Areias P, Rabczuk T. Steiner-point free edge cutting of tetrahedral meshes with applications in fracture. Finite Elements in Analysis and Design, 2017, 132: 27–41
33. Liu G, Zhuang X, Cui Z. Three-dimensional slope stability analysis using independent cover based numerical manifold and vector method. Engineering Geology, 2017, 225: 83–95
34. Zhang Y, Lackner R, Zeiml M, Mang H A. Strong discontinuity embedded approach with standard SOS formulation: Element formulation, energy-based crack-tracking strategy, and validations. Computer Methods in Applied Mechanics and Engineering, 2015, 287: 335–366
35. Zhang Y, Zhuang X, Lackner R. Stability analysis of shotcrete supported crown of NATM tunnels with discontinuity layout optimization. International Journal for Numerical and Analytical Methods in Geomechanics, 2018, 42(11): 1199–1216
36. Ren H, Zhuang X, Rabczuk T. Dual-horizon peridynamics: A stable solution to varying horizons. Computer Methods in Applied Mechanics and Engineering, 2017, 318: 762–782
37. Zhang Y, Zhuang X. Cracking elements: A self-propagating strong discontinuity embedded approach for quasi-brittle fracture. Finite Elements in Analysis and Design, 2018, 144: 84–100
38. Rabczuk T, Zi G, Bordas S, Nguyen-Xuan H. A simple and robust three-dimensional cracking-particle method without enrichment. Computer Methods in Applied Mechanics and Engineering, 2010, 199(37–40): 2437–2455
39. Zhang Y, Zhuang X. Cracking elements method for dynamic brittle fracture. Theoretical and Applied Fracture Mechanics, 2019, 102: 1–9
40. Zhang Y. Multi-slicing strategy for the three-dimensional discontinuity layout optimization (3D DLO). International Journal for Numerical and Analytical Methods in Geomechanics, 2017, 41(4): 488–507
41. Sloan S W. Upper bound limit analysis using finite elements and linear programming. International Journal for Numerical and Analytical Methods in Geomechanics, 1989, 13(3): 263–282
42. Areias P, Reinoso J, Camanho P P, César de Sá J, Rabczuk T. Effective 2D and 3D crack propagation with local mesh refinement and the screened Poisson equation. Engineering Fracture Mechanics, 2018, 189: 339–360
43. Rabczuk T, Belytschko T. Cracking particles: A simplified meshfree method for arbitrary evolving cracks. International Journal for Numerical Methods in Engineering, 2004, 61(13): 2316–2343
44. Ren H, Zhuang X, Cai Y, Rabczuk T. Dual-horizon peridynamics. International Journal for Numerical Methods in Engineering, 2016, 108(12): 1451–1476
45. Martínez-Galván S A, Romo M P. Assessment of an alternative to deep foundations in compressible clays: The structural cell foundation. Frontiers of Structural and Civil Engineering, 2018, 12(1): 67–80
46. Yang X, Han J, Parsons R L, Leshchinsky D. Three-dimensional numerical modeling of single geocell-reinforced sand. Frontiers of Architecture and Civil Engineering in China, 2010, 4(2): 233–240
47. Atkinson J. The Mechanics of Soils and Foundations. London: Taylor & Francis, 2007
48. Hicks M A, Samy K. Influence of heterogeneity on undrained clay slope stability. Quarterly Journal of Engineering Geology and Hydrogeology, 2002, 35(1): 41–49
49. Hamdia K M, Silani M, Zhuang X, He P, Rabczuk T. Stochastic analysis of the fracture toughness of polymeric nanoparticle composites using polynomial chaos expansions. International Journal of Fracture, 2017, 206(2): 215–227
50. Vu-Bac N, Lahmer T, Zhuang X, Nguyen-Thoi T, Rabczuk T. A software framework for probabilistic sensitivity analysis for computationally expensive models. Advances in Engineering Software, 2016, 100: 19–31
51. Das B M, Sobhan K. Principles of Geotechnical Engineering. California: Thomson Learning, 2013
52. Ortiz J M R, Gesta J S, Mazo C O. Infrastructure Application Course. Madrid: Publishing Office of the Official Institute of Architects, 1986 (in Spanish)